Materials Science Forum
ISSN: 1662-9752, Vol. 1183, pp 107-117
doi:10.4028/p-rRmI12

Submitted: 2026-01-25
Revised: 2026-02-21
Accepted: 2026-02-24
Online: 2026-04-13

Rolling-Induced Anisotropy in High-Cycle Three-Point Bending Fatigue of an AA7075-T6 Plate

Alexandros Prospathopoulos[1,2,a], Apostolos Argyros[1,2,b], Maria Pappa[1,2,c], Nikolaos Michailidis[1,2,d*]

[1]Physical Metallurgy Laboratory, Dept. of Mechanical Engineering, School of Engineering, Aristotle University of Thessaloniki, 54124 Thessaloniki, Greece

[2]Centre for Research & Development of Advanced Materials (CERDAM), Center for Interdisciplinary Research and Innovation (CIRI), Balkan Centre, Building B', 10th km Thessaloniki-Thermi Road, 57001, Thessaloniki, Greece

[a]alexpros@meng.auth.gr, [b]aargiros@auth.gr, [c]pappmari@auth.gr, [d*]nmichail@meng.auth.gr

*corresponding author

Keywords: AA7075-T6, rolling anisotropy, three-point bending, high-cycle fatigue, intermetallic particles, crack growth.

Abstract. Rolled 7xxx-series Al alloys exhibit pronounced microstructural anisotropy (pancake grains and intermetallic particles) that can strongly affect fatigue initiation and -crack growth. In the current study, an AA7075-T6 plate was examined in three orthogonal machining orientations-L–S (longitudinal), L–T (long-transverse) and T–S (short-transverse)-using high-cycle three-point bending fatigue at room temperature (R = 0, f = 25 Hz, σ_{max} = 360–400 MPa, i.e., ~0.79–0.88 σy). Optical/SEM observations reveal elongated grains and a grain-density gradient through thickness, accompanied by orientation-dependent distributions of intermetallic particles. Despite only small differences in monotonic response, fatigue performance is strongly orientation-dependent: the T–S specimens exhibit the longest lives in the S–N curves. Fractography and striation-based kinetics show the lowest Paris-regime crack-growth rate for T–S ($da/dN \approx 1.85\times10^{-7}$ m/cycle at $\Delta K \approx 10.5$ MPa√m), while L–S shows the fastest growth ($da/dN \approx 4.3\times10^{-7}$ m/cycle at $\Delta K \approx 13.0$ MPa√m). The improved T–S fatigue resistance is discussed in terms of crack-path interaction with grain boundaries and particle populations (coherent/penetrable vs non-coherent/coarse particles), which can either deflect/retard cracks or act as initiation sites. The results provide a compact microstructure–mechanics map for rolling-induced anisotropy in AA7075-T6 under bending fatigue.

Introduction

Aluminum alloys are extensively used in aviation thanks to their superior strength-to-density ratio. Over the years, numerous studies have investigated their fatigue behavior. This process involves crack initiation followed by propagation until failure [1]. Aluminum alloy 7075 is a preferred choice for aircraft structural components due to its exceptional strength-to-weight ratio [2].

AA7075 in the peak-aged (T6) condition is widely used in safety-critical lightweight structures because of its high specific strength. The same microstructural features that enable precipitation strengthening-fine η′/GP precipitates and dispersoids-coexist with coarse constituent particles (often Fe- and Cu-bearing) and rolling-induced pancake grains [3].

Constituent particles in this alloy exhibit wide variations in composition and structure. They are typically classified into two groups: those rich in Al, Cu, Mg, and Zn, and those containing Al, Fe, Cu, Mn, and Zn [4].

Harlow (2010) investigated the role of constituent particles in 7075-T651 aluminum alloy on the evolution of microstructurally small damage. The study concluded that fatigue damage nucleation and propagation in aluminum alloys involve complex stochastic processes. Constituent particles play a dominant role, with Fe-bearing particles being particularly critical due to local stresses, grain orientation, particle geometry, and possibly other material properties [5].

In Al-Zn-Mg-Cu alloys, brittle intermetallic phases—particularly coarse Fe-rich and Cu-containing particles such as $Al7Cu_2Fe$, Al_7Cu_2Fe and $Al_6(CuFe)$, $Al_6(CuFe)$—strongly influence fatigue crack propagation by serving as primary crack initiation sites. These particles fracture readily, inducing crack deflection and branching that initially retards growth but can reduce overall fracture toughness [6].

Espezua et. al. (2012) compared three 6xxx-series aluminum alloys to assess how intermetallics and precipitates affect fatigue crack nucleation. They concluded that mechanical stresses from transport vehicle operation induce material fatigue, resulting in crack nucleation primarily at inclusions, constituent particles, or precipitates, followed by propagation to fracture. The study identified intermetallic particles containing Fe, Mn, and Si as key nucleation sites, as both intermetallics and precipitates act as stress concentrators that readily initiate fatigue cracks [7].

Navaee (2021), in a study on asymmetric cold rolling of AA7075 aluminum alloy, demonstrated that brittle Fe-rich intermetallic particles serve as prime sites for crack initiation and propagation via particle fracture or interface decohesion [8].

The effects of aging on the microstructure and properties of 7075 Al sheets has been investigated by (Zhao, 2020). They showed that for 7075 alloy, a large amount of $MgZn_2$ (η) second-phase particles break during cold deformation [9].

A model to assess the influence of weak interface layers on the breaking of coarse constituent particles has been developed by Startik (2005). The researchers concluded that PFZs around particles can have an important influence on their failure in the presence of a stress field such as that caused by a loaded crack progressing through the material. The PFZ strengthen the material and thus PFZs around particles can be beneficial to damage tolerance [10].

Zhang et al. (2020) underscored the research challenge, noting that high-strength aluminum alloys suffer from notoriously poor fatigue performance. Engineers must therefore account for this limitation when designing to improve structural fatigue strength [11].

Leng et al. (2018) described two key models for precipitate-dislocation interactions: the dislocation cutting mechanism and the bypassing (Orowan) mechanism. These depend on precipitate size and coherency with the matrix [12].

Mbuya (2017) notes that although crack propagation through fractured particles occurs, it is less frequent and typically limited to thin, favorably oriented particles parallel to the loading direction [13].

Cold working and subsequent aging frequently align particles into stringers and generate three distinct planes (L–T, L–S and T–S), leading to direction-dependent fatigue initiation and short-crack propagation. While orientation effects have been reported for several Al alloys under bending fatigue, direct comparisons across all three orthogonal planes of a single AA7075-T6 plate under identical three-point bending conditions remain scarce.

The present study investigates the rolling-induced fatigue anisotropy of AA7075-T6 aluminum alloy, a material widely recognized for its exceptional strength-to-weight ratio and extensive applications in aerospace engineering. Despite extensive research on the fatigue behavior of aluminum alloys, a gap remains in comparative analyses that encompass all three orthogonal orientations under identical loading conditions. This study aims to fill that gap by providing a compact dataset that elucidates the anisotropic behavior of AA7075-T6, revealing critical insights into microstructural influences on fatigue performance combining (i) optical/SEM evidence of grain morphology and particle/crack interactions, (ii) basic mechanical metrics (elastic modulus, hardness and tensile response), and (iii) fatigue S–N behavior with striation-based estimates of Paris-regime crack growth. . By systematically comparing the fatigue life and crack growth rates across the longitudinal, long-transverse, and short-transverse orientations, we offer a comprehensive view that enhances both scientific understanding and practical engineering applications.

The goal is not an exhaustive parametric study, but a compact set of results that links orientation to fatigue performance through the most load-bearing microstructural mechanisms.

Materials and Methods

The material was supplied by the Hellenic Aerospace Industry. The specimens were machined from pieces of material with random dimensions, but these were sufficient to achieve the desired geometry. Processing was performed using shaping tools such as saws, lathes, milling machines, and drills.

For the experimental analysis, a total of 39 specimens were tested, with 13 specimens designated for each of the three orthogonal orientations: longitudinal (L–S), long-transverse (L–T), and short-transverse (T–S). Each orientation was subjected to different stress levels (σmax = 360-400 MPa) to comprehensively evaluate the fatigue behavior across varying loading conditions. This approach ensures robust statistical significance and enhances the transparency of the results presented.

A commercial rolled AA7075 plate in the T6 condition was examined. The processing sequence corresponds to solution treatment, quenching, cold rolling and artificial aging (Fig. 1).

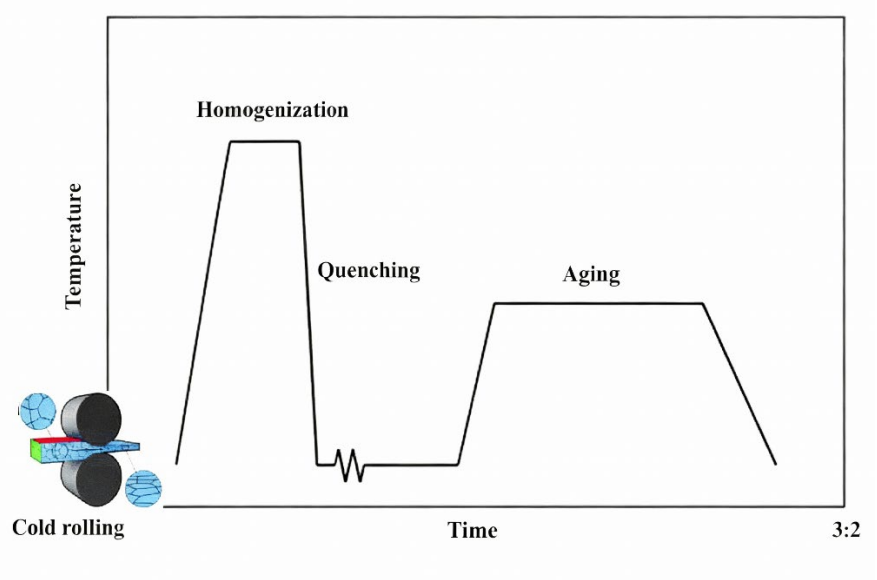

Fig. 1. Schematic heat-treatment sequence for AA7075-T6 (solution treatment → quench → cold rolling → aging).

Specimens were cut along the three orthogonal directions of the plate: L–S (longitudinal), L–T (long-transverse) and T–S (short-transverse) (Fig. 2).

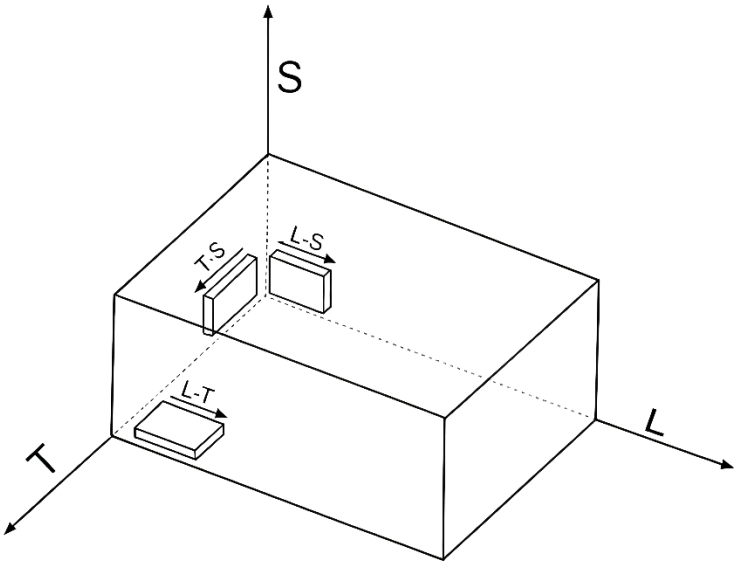

Fig. 2. Specimen geometry and orientation relative to the rolled plate: L–S, L–T, and T–S (three-point bending).

The rectangular fatigue coupons were machined to (70 mm x 10mm x 3mm) (L-T-S) dimensions were tested in three-point bending. The tensile surface (maximum tensile stress) was progressively ground using SiC papers (120 to 1200 grit) to minimize roughness-induced scatter.

Fatigue tests were performed at room temperature on a DMA ElectroForce 3550 (TA Instruments) at a frequency of 25 Hz and a stress ratio R = 0. The nominal maximum bending stress was set to σ_{max} = 360–400 MPa (approximately 0.79–0.88 of the yield stress reported for this material). For a rectangular section, the applied load was calculated from the standard three-point bending relation (Eq.1):

$$F=(\sigma*2b*d^2)/3L \ [N] \quad (1)$$

Where F is the applied force, L the span, and b and d the specimen width and thickness, respectively.

Microstructure and fracture surfaces were examined by optical microscopy and SEM equipped with EDS. Elastic modulus and tensile stress–strain curves were used to check for orientation-dependent monotonic response. Microhardness profiles across the thickness of cracked specimens were also measured to assess local work/strain-hardening trends between compression and tension sides.

Results

Microstructure and orientation-dependent features

Optical microscopy confirms the expected rolled-plate morphology: grains are elongated along the rolling direction and exhibit a pronounced gradient in grain density and thickness through the plate thickness. Representative views for the L–S and T–S planes are shown in Fig. 3 and Fig. 4.

The methodology for quantitative grain-width analysis entailed the following: Samples from L–S, L–T, and T–S orientations were sectioned and prepared by grinding, polishing and etched with Keller's reagent to reveal grain boundaries. Five representative optical microscope images per orientation (magnification 100×) were selected via random sampling across the gauge length to minimize bias. Using Image-J software, grain widths were measured as the mean intercept length perpendicular to the rolling direction: at least 20 test lines (spaced 2 μm apart) were overlaid per image, with intercepts counted only at fully traversed grains.

The above quantitative image analysis reveals a markedly larger mean grain width for the L–T plane (≈1.34×10^5 nm) compared to L–S (≈4.50×10^4 nm) and T–S (≈3.54×10^4 nm), with the strongest spatial variation observed toward the tensile surface (Fig. 5). Intermetallic particles are frequently observed along subgrain boundaries and in stringers, and SEM fractography reveals both crack-deflection/retardation at certain particles and crack-bridging pathways created by fractured particle fragments (Fig. 9–10).

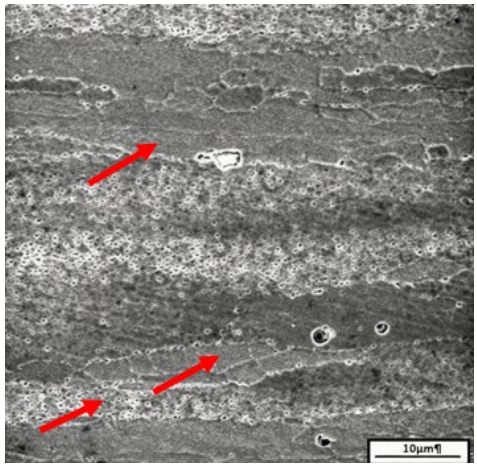

Fig. 3. Representative optical micrograph showing elongated grains and particle distribution in the rolled plate (example: L–S plane).

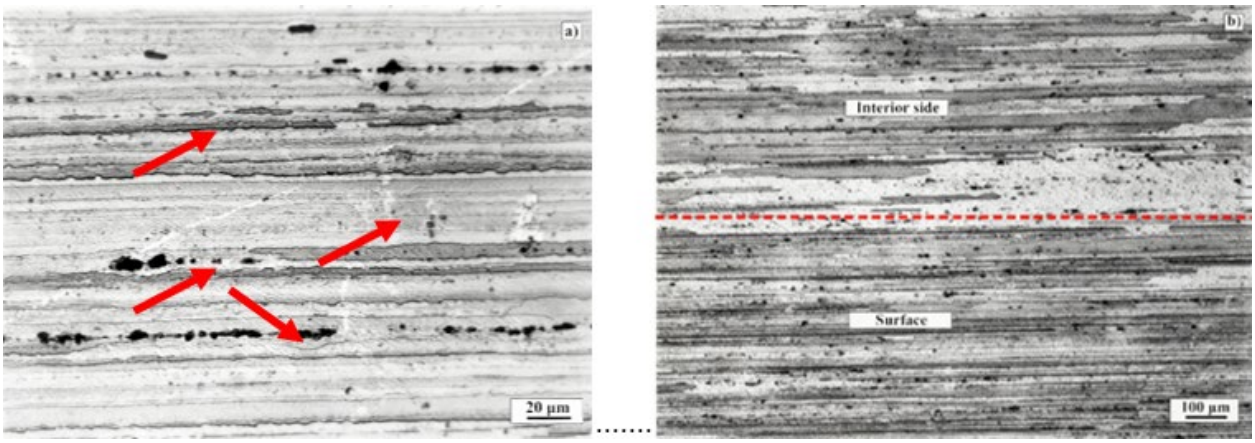

Fig. 4a. Elongated grains along the L-S plane, b) Non uniform grains density between the interior and the surface of the (L-S) samples.

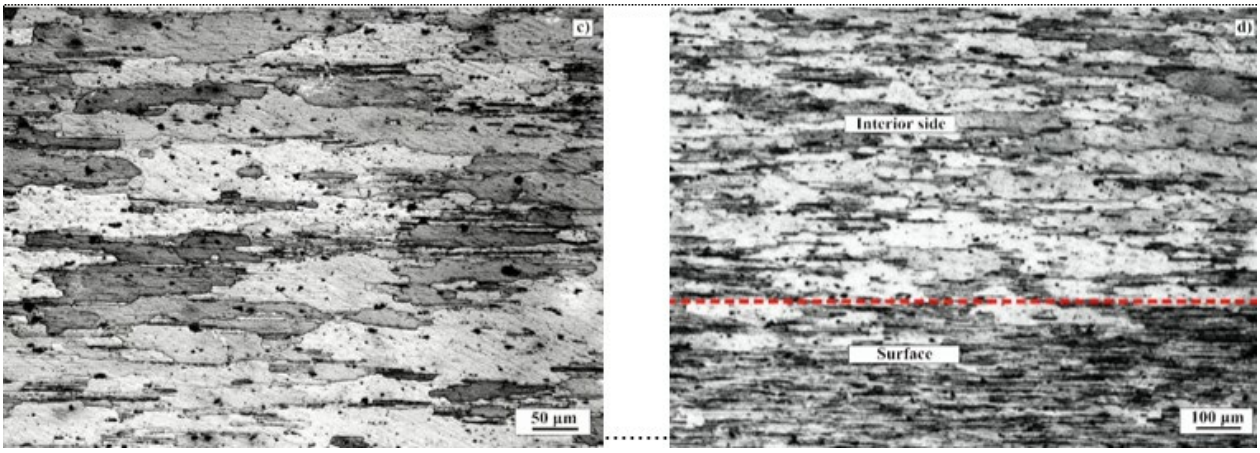

Fig. 4b. Grain morphology in the T–S plane (two magnifications).

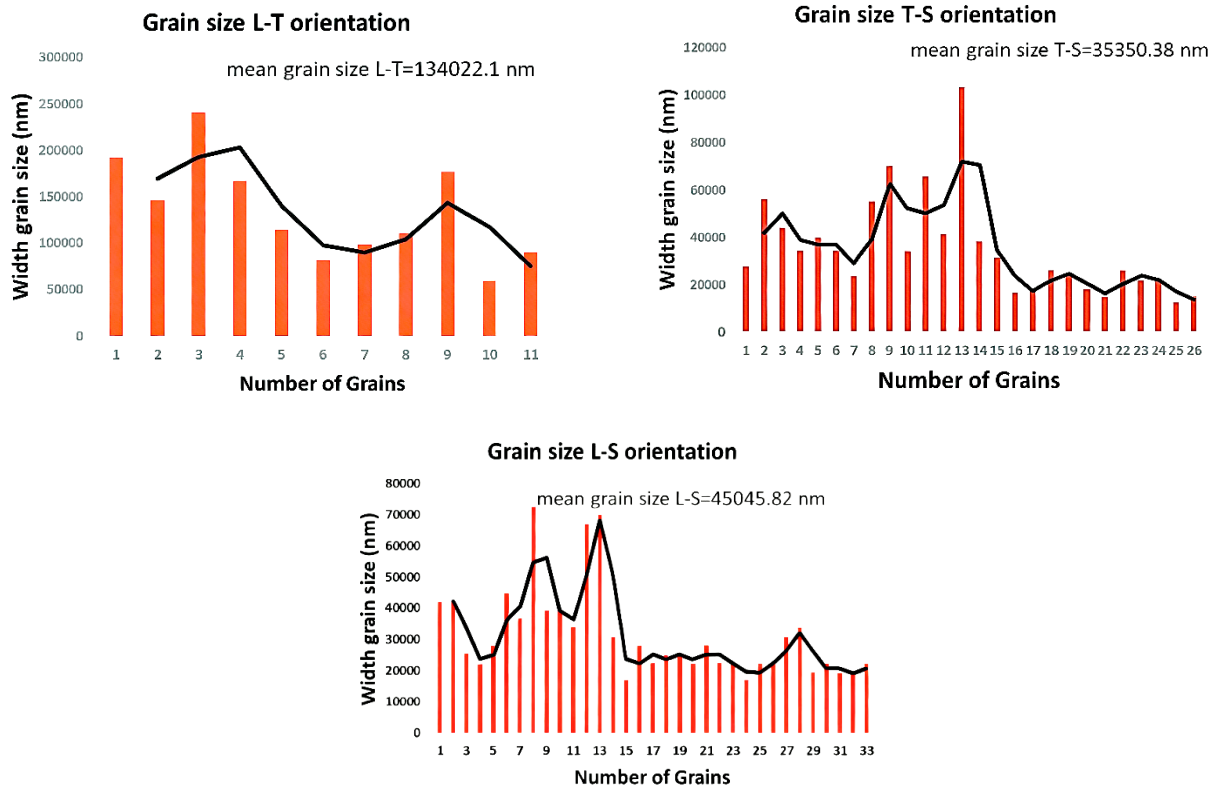

Fig. 5. Quantified grain-width variation across orientations (mean values indicated on plots).

Mechanical response (elastic modulus, tensile behavior and hardness trends)

Elastic modulus exhibits a clear orientation dependence (Fig. 6): T–S shows a lower modulus than L–S and L–T. Consistently, tensile curves indicate slightly higher tensile strength but reduced elongation in T–S compared with the other two directions. Microhardness profiles across cracked specimens increase from the compression side toward the tensile side, consistent with a non-uniform through-thickness deformation state under bending and with the observed grain-thickness gradient.

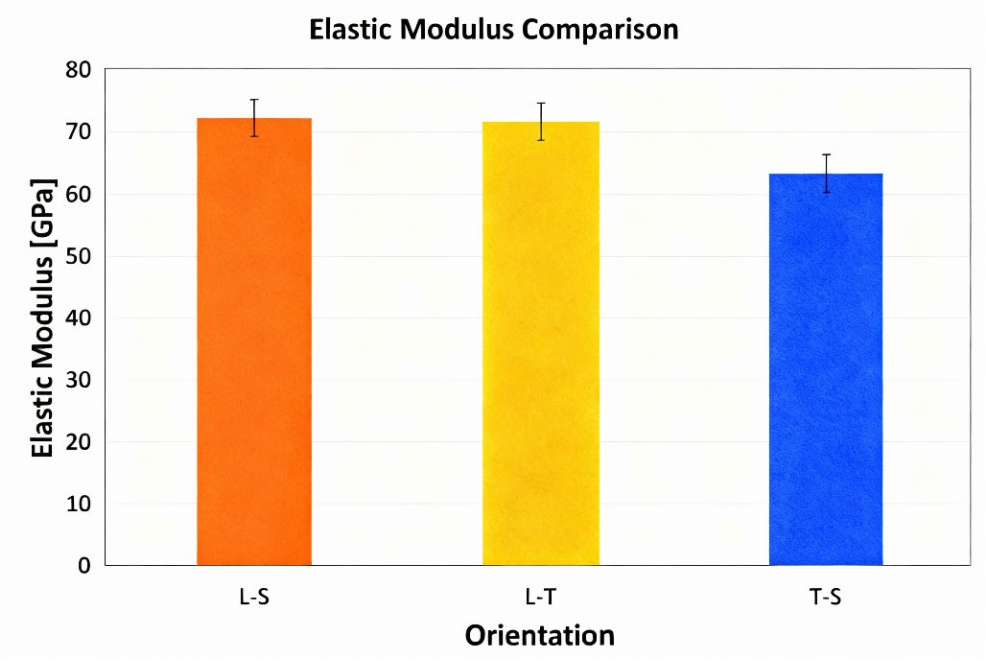

Fig. 6. Elastic modulus of AA7075-T6 in the three orientations (lower modulus in T–S).

High-cycle fatigue (S–N curves)

Fig. 7 illustrates only a representative part of the S-N curve to highlight the differences in fatigue life of the three orientations. A pronounced anisotropy is observed: the short-transverse T–S orientation consistently provides the longest fatigue life, followed by L–T, while L–S shows the shortest life within the investigated stress range. The life scatter is typical for high-strength Al alloys, where crack initiation is highly sensitive to the presence and location of coarse particles, near-surface defects and local surface conditions.

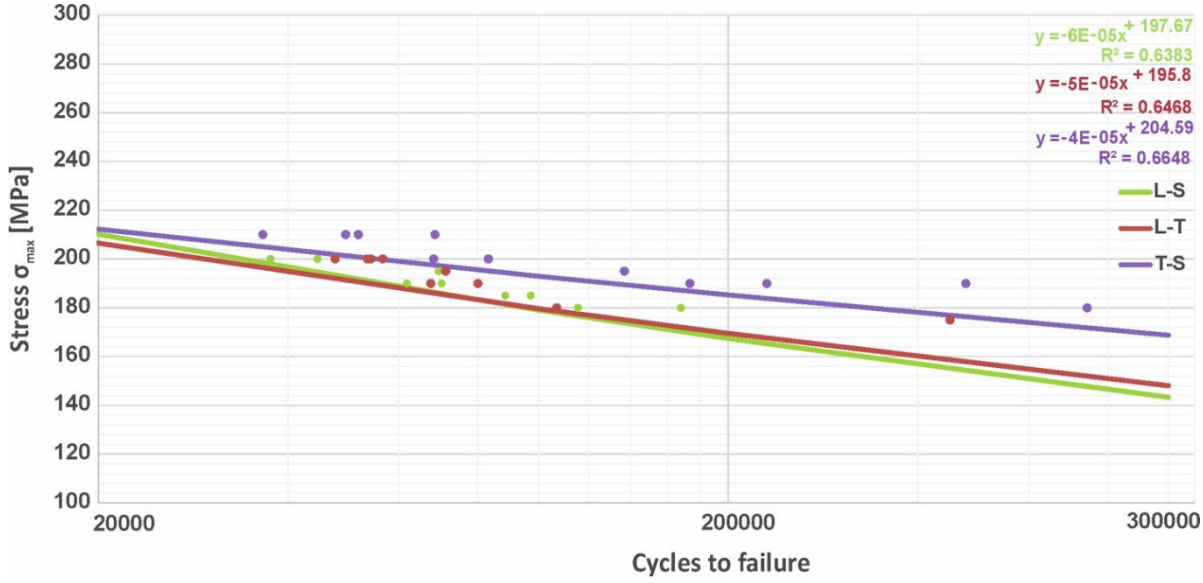

Fig. 7. S–N curves for AA7075-T6 in L–S, L–T and T–S orientations under three-point bending fatigue.

The standard deviations for each orientation is: σ (T-S)= 234.383 cycles, σ (L-S)=38.048 cycles, σ (L-T)= 128.886 cycles. The following example illustrates the calculation of the standard deviation for the L-S orientation using the formulas (2),(3):

$$\mu_{(L-S)} = \frac{\Sigma x_i}{N} \quad (2)$$

Where: x_i=individual fatigue life values
$\mu_{(L-S)}$=mean of the values
N=total number of values

$$\sigma_{(L-S)} = \sqrt{\frac{\Sigma (x_i - \mu_{(L-S)})^2}{N-1}} \quad (3)$$

Where: $\sigma_{(L-S)}$=standard deviation
L-S: Mean = 82422 [N], L-T: Mean =109705 [N], T-S: Mean = 188790 [N]
$\mu_{(L-S)}$=[37536+44583+70141+61764+168269+115427+71348+69455+97182+88517]/10=82422.

Crack-growth kinetics from striation measurements

To rationalize the orientation dependence beyond initiation, crack-growth rates were estimated from SEM striation spacing, assuming one striation per cycle. Table 1 summarizes the corresponding Paris-regime values, together with the stress-intensity factor ranges reported for each orientation. The T–S specimens exhibit the lowest ΔK and the slowest crack growth, consistent with their longer fatigue life. The crack-growth rates presented in this study were derived from striation spacing measurements, assuming a one-to-one relationship where one striation corresponds to one loading cycle. It is essential to frame these rates as semi-quantitative estimates due to several simplifying assumptions inherent in this method. One of them is the uniform distribution of striations along the fracture surface and the exclusion of potential variations in loading conditions during crack propagation.

Table 1. Striation-based crack-growth rates in the Paris regime ($da/dN = C(\Delta K)^n$ with $C = 3\times10^{-11}$ and $n = 3.7$).

Orientation	Striations (count / 10 μm)	da/dN (m/cycle)	ΔK (MPa√m)
L–S	23 / 10	4.3×10^{-7}	13.02
L–T	39 / 10	2.56×10^{-7}	11.5
T–S	54 / 10	1.85×10^{-7}	10.5

The stress intensity factor ΔK was calculated using an equation proposed by Paris and Erdogan for measuring the crack propagation rate, which is based on assumptions regarding the crack lengths that were indirectly measured rather than directly observed. This introduces inherent uncertainties, as the accuracy of ΔK is contingent upon the validity of these assumptions. Variations in crack morphology and the effects of microstructural features on crack propagation can further contribute to discrepancies between calculated and actual ΔK values. Therefore, it is important to interpret the ΔK results with caution, recognizing these limitations in the context of the overall findings [14]. Fig. 8 shows an indicative example of measuring the crack growth rate using ImageJ software.

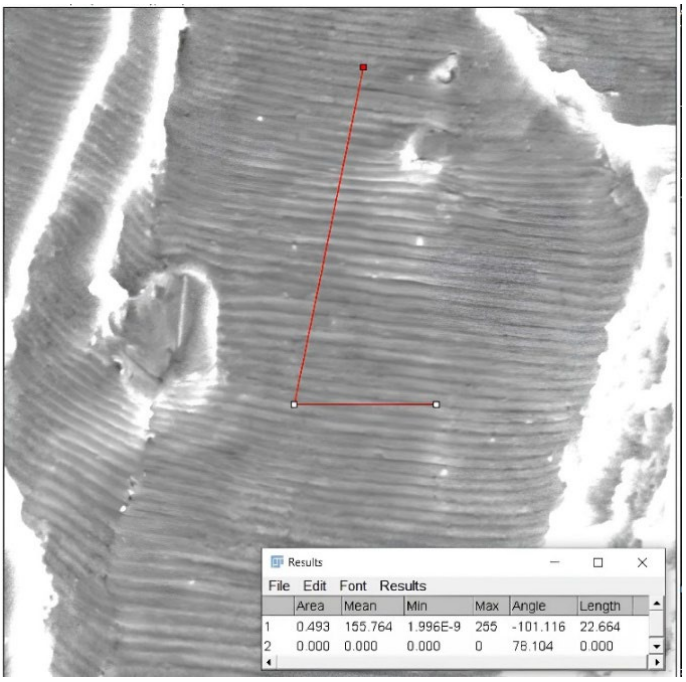

$$\text{(L-S)}\ \frac{da}{dN} = C(\Delta K)^m \Longrightarrow$$

$$\boxed{\Delta K = 14.18\text{MPa}\sqrt{m}}$$

Fig. 8. Example of crack growth rate measurement.

Fractography: particle–crack interactions

SEM observations emphasize the dual role of intermetallic particles. In some cases, particles act as effective obstacles that deflect and retard the crack (Fig. 9). In others, fractured particles and their fragments create local microcracks and bridge across adjacent grains, providing a preferential pathway for crack advance (Fig. 10). This balance between barrier and weak-path behavior depends on particle size, coherency with the matrix, and their orientation relative to the crack plane.

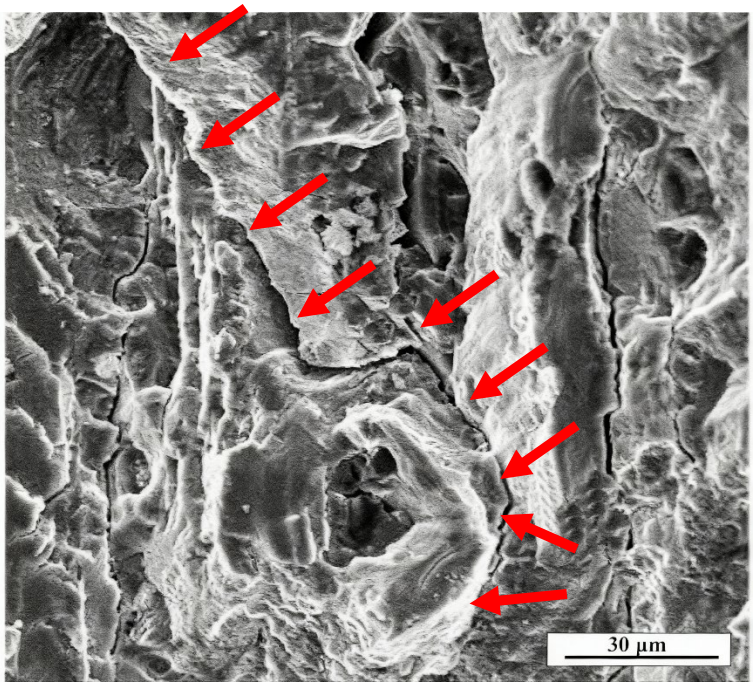

Fig. 9. Example of crack retardation/deflection at an intermetallic particle (T–S specimen).

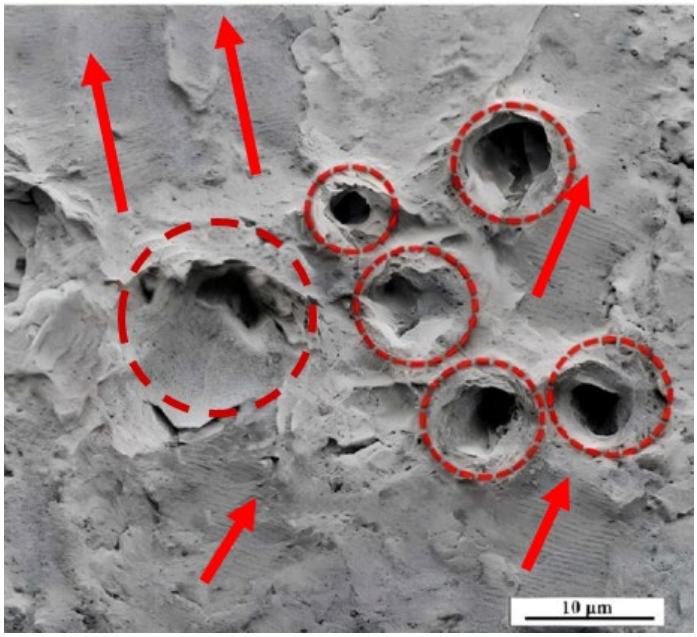

Fig. 10. Intermetallic particle fragments acting as crack bridges/pathways (L–S specimen).

Crack initiation and propagation originate from distinct mechanisms. Initiation generally starts at microstructural defects or stress concentrators—like inclusions, grain boundaries, or intermetallic particles-and depends on factors such as microstructural heterogeneity and applied loading conditions.

Propagation, however, is controlled by the material's fracture toughness and crack growth mechanisms, which are dictated by local microstructure and stress intensity factors at the crack tip.

Discussion

The present study highlights an important practical point: in a rolled AA7075-T6 plate, the fatigue ranking under three-point bending can differ from the ranking expected from monotonic strength alone. The elastic modulus and tensile strength vary only modestly with orientation, yet fatigue life changes markedly.

A consistent interpretation emerges when considering the crack path relative to (i) the pancake-grain architecture and (ii) the alignment of particle stringers introduced by rolling. In orientations where the crack front intersects a higher density of grain boundaries and particle bands at high angles, local stress concentrations at particles and interfaces promote earlier microcrack coalescence and faster short-crack propagation. Conversely, the improved T–S performance is compatible with a crack path that encounters fewer effective barriers/weak interfaces per unit advance, leading to a lower effective driving force (lower ΔK) and slower Paris-regime growth (Table 1).

Particle coherency further modulates this behavior. Coherent or semi-coherent precipitates (often termed ‘penetrable’) can strengthen the matrix and contribute to crack blunting/deflection, whereas coarse non-coherent particles and debonded interfaces can serve as dominant initiation sites. The SEM examples in Fig. 8–9 illustrate both mechanisms in the same alloy. From an engineering perspective, these findings reinforce that fatigue design in 7xxx alloys should treat orientation as a first-order variable and should control near-surface particle populations and surface preparation to reduce initiation sensitivity.

Key contributions of this scientific study:

• Direct, side-by-side comparison of all three orthogonal planes of a rolled AA7075-T6 plate under identical three-point bending fatigue loading.

• Coupled S–N ranking with striation-derived crack-growth kinetics, showing that the longest-life orientation (T–S) also exhibits the lowest ΔK and slowest Paris-regime growth.

• Mechanism-level fractography demonstrating the dual role of intermetallic particles as both crack barriers and weak paths via fracture/debonding and crack bridging.

Conclusion

Rolled AA7075-T6 exhibits pronounced microstructural anisotropy (pancake grains and intermetallic particles), which translates into strong fatigue anisotropy under three-point bending.

Within σ_{max} = 360–400 MPa (R = 0, f=25 Hz), the fatigue life ranks as T–S (longest) > L–T > L–S (shortest).

Elastic modulus is lowest in T–S, while tensile curves show only small differences in strength/ductility; fatigue performance cannot be inferred from monotonic response alone.

Striation-based kinetics indicate the slowest Paris-regime crack growth for T–S ($da/dN \approx 1.85\times10^{-7}$ m/cycle, $\Delta K \approx 10.5$ MPa$\sqrt{m}$) and the fastest for L–S ($da/dN \approx 4.3\times10^{-7}$ m/cycle, $\Delta K \approx 13.0$ MPa$\sqrt{m}$).

Fractography confirms a dual particle role: certain particles deflect/retard cracks, whereas fractured/debonded particles provide initiation sites and crack-bridging pathways. The orientation-dependent crack interaction with grain boundaries and particle alignment rationalizes the observed S–N ranking.

Summarizing, we would say that this study presents a comparative analysis of rolling-induced anisotropy in AA7075-T6 aluminum alloy across three orthogonal orientations: longitudinal (L–S), long-transverse (L–T), and short-transverse (T–S).

Unlike previous studies that often focus on isolated orientations or lack direct comparisons, our approach facilitates a comprehensive understanding of how microstructural features influence fatigue performance under identical loading conditions, which constitutes a valuable resource for engineers researching the optimization of aeronautical aluminum alloys.

References

[1] Y. Zhao, T., Jiang, Fatigue of 7075-T651 aluminum alloy, Int. J. Fatigue, vol. 30, no. 5, pp. 834–849, (2008).

[2] J.Park, Influence of Retrogression and Reaging Treatments on the Strength and Stress Corrosion Resistance of Aluminium Alloy 7075-T 6, Mater. Sci. Eng., vol. A103, pp. 223–231, (1988).

[3] B. Dalai, Moretti M.A., P. Akerstrom, C. Arvieu, D. Jacquin, L.-E. Lindgren, Mechanical behavior and microstructure evolution during deformation of AA7075-T651, Materials Science & Engineering A, vol.822, p.p.141615. (2021).

[4] W. Harlow, D.G., Wang, M.Z., Statistical Analysis of Constituent Particles in 7075-T6 Aluminum Alloy, Metall. Mater. Trans. A, vol. 37A, pp. 3367–3373, (2006).

[5] D. G. Harlow, J. Nardiello, and J. Payne, The effect of constituent particles in aluminum alloys on fatigue damage evolution: Statistical observations, Int. J. Fatigue, (2010), doi: 10.1016/j.ijfatigue.2009.02.036.

[6] Z. Vratnica, Z. Cvijović, K. Gerić, The Role of Intermetallic Phases in Fatigue Crack Propagation Behavior of Al-Zn-Mg-Cu Alloys, Mater. Sci. Forum, vol. 555, pp. 553–558, (2007).

[7] A. Espezua, S., Baptista, C., Laurito, D., and da Silva, Influence of Intermetallics and Precipitates on the Fatigue Crack: Nucleation And Propagation in Aluminum Alloys 6005-T6, 6063-T6 and 6351-T6, SAE Tech. Pap., (2012), [Online]. Available: https://doi.org/10.4271/2012-36-0520.

[8] J. A. K. Navaee, R. Jamaati, Asymmetric cold rolling of AA7075 alloy: The evolution of microstructure, crystallographic texture, and mechanical properties, Mater. Sci. Eng. A, vol. 824, (2021).

[9] F.Zhao, R. Wu , B. Wang , M. Huang , G. Lei, Effects of Aging on the Microstructure and Properties of 7075 Al Sheets, materials\, vol. 13, no. 18, (2020), [Online]. Available: doi: 10.3390/ma13184022.

[10] M. J. Starink, Reduced fracturing of intermetallic particles during crack propagation in age hardening Al-based alloys due to PFZs, Mater. Sci. Eng. A, vol. 390, no. 1–2, (2005).

[11] C. Zhang, Q., Zhu Y., Gao, X., Wu, Y., Hutchinson, Training high-strength aluminum alloys to withstand fatigue, Nat. Commun., vol. 11, no. 5198, (2020).

[12] Z., Leng and .Q. Duan, P. Zhang, Improving the fatigue strength of 7075 alloy through aging, Mater. Sci. Eng. A, vol. 738, pp. 24–30, (2018), [Online]. Available: https://doi.org/10.1016/j.msea.2018.09.047.

[13] T. Mbuya, Y. Gu, R. C. Thomson, Effect of intermetallic particles and grain boundaries on short fatigue crack growth behaviour in a cast Al–4Cu–3Ni–0.7Si piston alloy, Fatigue Fract. Eng. Mater. Struct., (2017).

[14] P. Xrisoulakis, *Materials Science and Engineering*. Athens, 2008.